PCCP

ROYAL SOCIETY OF CHEMISTRY

PAPER

View Article Online
View Journal | View Issue

Cite this: *Phys. Chem. Chem. Phys.*, 2023, **25**, 29951

N,S coordination in Ni single-atom catalyst promoting CO_2RR towards HCOOH†

Zengxuan Chen,[a] Shoufu Cao,[a] Jiao Li,[a] Chunyu Yang,[a] Shuxian Wei,[b] Siyuan Liu,[a] Zhaojie Wang *[a] and Xiaoqing Lu *[a]

Received 4th August 2023,
Accepted 16th October 2023

DOI: 10.1039/d3cp03722c

rsc.li/pccp

Carbon-based single atom catalysts (SACs) are attracting extensive attention in the CO_2 reduction reaction (CO_2RR) due to their maximal atomic utilization, easily regulated active center and high catalytic activity, in which the coordination environment plays a crucial role in the intrinsic catalytic activity. Taking NiN_4 as an example, this study reveals that the introduction of different numbers of S atoms into N coordination (Ni–N_xS_{4-x} (x = 1–4)) results in outstanding structural stability and catalytic activity. Owing to the additional orbitals around −1.60 eV and abundant Ni d_{xz}, d_{yz}, d_{x^2}, and d_{z^2} orbital occupation after S substitution, N,S coordination can effectively facilitate the protonation of adsorbed intermediates and thus accelerate the overall CO_2RR. The CO_2RR mechanisms for CO and HCOOH generation *via* two-electron pathways are systematically elucidated on NiN_4, NiN_3S_1 and NiN_2S_2. NiN_2S_2 yields HCOOH as the most favorable product with a limiting potential of −0.24 V, surpassing NiN_4 (−1.14 V) and NiN_3S_1 (−0.50 V), which indicates that the different S-atom substitution of NiN_4 has considerable influence on the CO_2RR performance. This work highlights NiN_2S_2 as a high-performance CO_2RR catalyst to produce HCOOH, and demonstrates that N,S coordination is an effective strategy to regulate the performance of atomically dispersed electrocatalysts.

1. Introduction

The electrocatalytic CO_2 reduction reaction (CO_2RR) is a promising and effective strategy for addressing CO_2 emissions and producing high-added-value fuels and chemicals.[1–3] The chemical inertness of CO_2 makes it difficult to convert; thus, exploring appropriate catalysts to break the high-energy C=O bond and generate specific products in the CO_2RR is particularly critical.[4] A plethora of CO_2RR electrocatalysts have been extensively designed and investigated to achieve exceptional catalytic activity, superior selectively, and good stability to meet the demands of industrial-scale production.[5,6] Recently, single-atom catalysts (SACs) have attracted great attention because of their remarkable catalytic activity, maximal atomic utilization, easily regulated active center and low cost.[7–9] In carbon-based SACs, N coordinated structures provide a plethora of possible active sites on which to anchor metal atoms.[10–12] Numerous studies have shown that carbon-based SACs exhibit excellent CO_2RR performance. Fe-NC was observed to exhibit a dramatic increase in CO_2RR activity and could reach a CO selectivity of over 80% at a current density of 35 mA cm^{-2}.[13–15] Co-NC has exhibited a relatively low limiting potential in the CO_2RR and was predicted to have the potential to convert CO_2 into the products CO and HCOOH.[16] Ni-NC catalysts have exhibited unique reactivity and faradaic efficiency in converting CO_2 into CO, especially compared to Au- and Ag-based catalysts.[17,18] After 100 h of continuous reaction at CO formation current densities of up to 22 mA cm^{-2}, Ni-NC could maintain 98% selectivity toward CO.[19] In addition to the metal active centers, the regulation of the coordination environment by heteroatoms may also have significant effects on the catalytic properties of SACs.[20] The introduction of S atoms into N coordination allows for electron structure modulation of the active sites, which could facilitate the protonation of reaction intermediates as well as the overall CO_2RR process.[21] Lu *et al.* found that doping S atoms into the N coordination of Ni-SACs could improve their CO reduction efficiency and stability, allowing them to remain stable for 19 h without apparent activity decay. They demonstrated that the introduction of S heteroatoms could reduce the electron supply of Ni to the coordinating N atoms and contribute to the overall higher CO_2RR selectivity.[22] Jia *et al.* observed that the introduction of S atoms could tune the local electronic density of the Ni-NC catalysts, which was conducive to reducing the energy barriers for the reduction of CO_2 to CO.[23] Although previous studies of CO_2RR to give CO on

[a] *School of Materials Science and Engineering, China University of Petroleum, Qingdao, Shandong 266580, P. R. China. E-mail: wangzhaojie@upc.edu.cn, luxq@upc.edu.cn*

[b] *College of Science, China University of Petroleum, Qingdao, Shandong 266580, P. R. China*

† Electronic supplementary information (ESI) available. See DOI: https://doi.org/10.1039/d3cp03722c

Ni-SACs have been attempted, research on the effect of the number of coordinated S atoms in Ni-SACs on CO_2RR performance has not been systematically reported. In addition, detailed information involving the structural stability, electronic structure, and two-electron pathways of the CO_2RR to give CO and HCOOH on Ni-SACs with N,S coordination needs to be systematically provided.

In this work, based on density functional theory (DFT) calculations, we have comprehensively investigated the CO_2RR performances of a series of Ni–N_xS_{4-x} (x = 1–4) structures to evaluate the promotion effect of N,S coordination. First, the optimized structures of Ni–N_xS_{4-x} were determined, and their stability and electronic structures, including charge density differences as well as electronic density of states, were analyzed. Subsequently, the CO_2RR mechanisms to give CO and HCOOH *via* two-electron pathways were illustrated. Finally, the limiting potential was measured as a descriptor to evaluate the CO_2RR activity and selectivity over the competing hydrogen evolution reaction (HER) on NiN_4, NiN_3S_1 and NiN_2S_2. Results of this work highlighted the N,S synergistic effect on SACs in CO_2RR by tuning the coordination environment and provided an effective strategy to design ideal electrocatalysts.

2. Computational details

2.1 Simulation details

All calculations were carried out using spin-polarized DFT as implemented in Vienna *ab initio* simulation package (VASP) 6.1.0[24] with the Perdew–Burke–Ernzerhof (PBE)[25] generalized gradient approximation (GGA). The cutoff energy was set as 420 eV. To avoid the interaction of periodic units, the thickness of the vacuum layer was set to 15 Å. The *K*-points were set to 3 × 3 × 1 for geometry optimization and 15 × 15 × 5 for accurate electronic density of state calculations. The electronic energy and forces for structural optimization were converged to within 1.0×10^{-5} eV and 0.02 eV $Å^{-1}$. The electronic energy for frequency calculation was converged to within 1.0×10^{-7} eV. DFT energies were converted into free energies at 298.15 K using vibrations obtained from the VASP calculations with IBRION = 5. The van der Waals interactions were considered using the Grimme (DFT-D3) method.[26] The effect of the solvent was taken into consideration using the VASP implicit solvent model. Electric fields with counter charge were considered using VASPsol to consider the effect of electrochemical double layers.[27] VASPsol set a continuum charge distribution in the vacuum region of the cell with a positive or negative charge.[28] The non-electrostatic parameter TAU was set as zero to avoid numerical instabilities, in accordance with recent published works.[29] The continuum charge was sampled as 0, 0.50, 1.00, and 1.50 e to simulate different electric field intensities. The famous work by Peterson *et al.*[30] indicated that the PBE functional can cause errors in the total energy of gas molecules. Thus, a correction of +0.45 eV was applied to CO_2 in the current study.

2.2 Computational hydrogen electrode model

The computational hydrogen electrode (CHE) model[31] was employed to determine the changes in the Gibbs free energy (ΔG), in which the reaction: H^+ (aq) + e^- = 1/2 H_2 (g) was equilibrated at 0 V *versus* the reversible hydrogen electrode (RHE). ΔG for each elementary step was defined as follows:

$$\Delta G = \Delta E + \Delta E_{ZPE} + \int C_p dT - T\Delta S + \Delta G_U + \Delta G_{pH}$$

where ΔE is the electronic energy directly obtained from DFT calculations, ΔE_{ZPE}, $\int C_p dT$, and ΔS are the zero-point energy, enthalpic temperature correction, and the entropy difference between the products and the reactants, which were calculated based on the vibration analysis and employed to transform the electronic energies into free energies at room temperature (T = 298.15 K), respectively. The computational hydrogen electrode (CHE) model was also employed to determine the reaction energies as a function of the potential with a proton–electron pair in the reactant. The chemical potential of the proton and electron could be related to that of H_2 at 0 V *versus* the standard hydrogen electrode (SHE):

$$\mu_{H^+} + \mu_{e^-} = \frac{1}{2}\mu_{H_{2(g)}}$$

The surface charge inducing interfacial field effect was also added to the reaction energy,[32] which was expressed as

$$\Delta G(U) = \Delta G^\circ + \Delta G_U + \Delta G_{field}$$

where ΔG° is the free energy for the reaction at the potential of zero charge, and ΔG_U and ΔG_{field} are the contributions of the applied electrode potential and electric field, respectively. Chan *et al.* have demonstrated surface charge density as an appropriate descriptor for the electrostatic effects of the double layer on reaction energies, which describes the variations of the interfacial field local to the reaction plane.[11,33] Here, we relate the surface-charge density σ-dependent energies to the potential-dependent energies through the differential Helmholtz capacitance C_H and potential of zero charge ϕ_{PZC} as follows:

$$\varphi = \frac{1}{C}\sigma + \varphi_{PZC}$$

where the values of C_H and the potential of zero charge ϕ_{PZC} are 21 μF cm^{-2} and −0.07 V *vs.* SHE.[11] Thus, the added continuum charges of 0, 0.50, 1.00, and 1.50 e were converted to potentials of 0 V, −0.23 V, −0.54 V, and −0.84 V *vs.* SHE. For the vibration analysis of intermediate states, frequencies were calculated by treating all 3*N* degrees of the adsorbates as vibrational in the harmonic oscillator approximation, and the vibrations of the substrate surface were negligible. The potential limiting step (PLS) referred to the reaction step with the largest ΔG (ΔG_{max}). The limiting potential (U_L) was defined by the equation $U_L = -\Delta G_{max}/|e|$, where ΔG_{max} was the free energy change in the PLS.[30,34,35]

2.3 Structural stability calculation

The cohesive energies were defined as $E_{coh} = (n_C E_C + n_N E_N + n_S E_S + E_{Ni} - E_{base})/(n_C + n_N + n_S + 1)$, where n_C, n_N, and n_S denote the numbers of C, N, and S in the SACs, respectively; E_C, E_N, E_S, and E_{Ni} are the DFT energies of single C, N, S, and Ni atoms, respectively. The positive E_{coh} values indicated the considerable thermodynamic stability. The formation energies were calculated using the equation $E_f = E_{Ni@SUB} - E_{SUB} - E_{Ni}$, where $E_{Ni@SUB}$ is the total energy of the SAC, E_{Ni} is the DFT energy of the Ni atom, and E_{SUB} is the energy of the substrate. The negative E_f values indicated favorable synthetic feasibility. The dissolution potentials were calculated using the equation $U_{diss} = U^0_{diss}(\text{metal, bulk}) - E_f/eN_e$, where $U^0_{diss}(\text{metal, bulk})$ and N_e represent the standard dissolution potential of the bulk metal and the number of electrons involved in the dissolution. All the $U^0_{diss}(\text{metal, bulk})$ and N_e values refer to the values in Guo's previous studies.[36] The positive U_{diss} values indicated the superior electrochemical stability under CO_2RR conditions.

3. Results and discussion

3.1 Structure and stability

To investigate the effect of N,S cocoordination on Ni SACs, we systematically examined the Ni–N_xS_{4-x} (x = 1–4) structures. Fig. 1 shows the stable configurations of NiN_4, NiN_3S_1, and NiN_2S_2. The optimized configurations of NiN_2S_2-1, NiN_1S_3, and NiS_4 are provided in Fig. S1 in the ESI.† The lattice parameters of the NiN_4 structure were optimized to be 9.84 × 12.78 × 15.06 Å with all atoms in the same plane. For NiN_3S_1, one of the N atoms in NiN_4 was substituted by a S atom; the Ni–N distance was elongated to 1.884 from 1.872 Å in NiN_4, and the Ni–S length was 2.075 Å. Ni–N_2S_2 was subdivided into NiN_2S_2 and NiN_2S_2-1 according to the position of the two S atoms, where NiN_2S_2 and NiN_2S_2-1 represent para substitution and *ortho* substitution. For NiN_2S_2, two opposing N atoms in NiN_4 are substituted by two S atoms; the Ni–N length is 1.928 Å and the Ni–S length is 2.046 Å. For NiN_2S_2-1, two neighboring N atoms in NiN_4 are substituted by two S atoms; the Ni–N length is 1.874 Å and the Ni–S length is 2.116 Å. In NiN_1S_3, the Ni–N length is 1.977 Å and the Ni–S length is 2.153 Å. For NiS_4, the Ni–S length is 2.137 Å. These configurations are all distorted, resulting in a non-coplanar framework with the surrounding ligands, except in the case of NiN_4. The non-coplanar framework and the changes in the lengths of Ni–N and Ni–S are mainly caused by the larger atomic radius of the S atom compared to that of the N atom.

The synthetic feasibility, thermodynamic stability, and electrochemical stability of the structures were evaluated using the formation energy E_f, cohesive energy E_{coh}, and dissolution potential U_{diss}, respectively. The values of E_f were observed to be −6.39, −4.57 and −2.62 eV for NiN_4, NiN_3S_1, and NiN_2S_2, as shown in Table S1 in the ESI.† The E_f values of NiN_2S_2-1, NiN_1S_3, and NiS_4 are all less than zero. More negative E_f values indicate more favorable synthetic feasibility; thus, the synthetic feasibility follows the sequence NiN_4 > NiN_3S_1 > NiN_2S_2-1 > NiS_4 > NiN_2S_2 > NiN_1S_3. The values of E_{coh} are 9.03, 8.89, 8.76, 8.78, 8.64, and 8.52 eV for NiN_4, NiN_3S_1, NiN_2S_2, NiN_2S_2-1, NiN_1S_3, and NiS_4, respectively, demonstrating that these structures are all thermodynamically stable. The values of U_{diss} are 2.93, 2.02, 1.05, 1.93, 0.88, and 1.09 V on NiN_4, NiN_3S_1, NiN_2S_2, NiN_2S_2-1, NiN_1S_3, and NiS_4, respectively. A more positive U_{diss} demonstrates that the metal atoms can bind strongly with the substrate and can be prevented from dissolution, which endows higher stability under electrochemical conditions. Analyses of the formation energy, cohesive energy, and dissolution potential suggest that these configurations are all stable. Comparatively, NiN_4, NiN_3S_1, and NiN_2S_2 are much more stable than NiN_2S_2-1, NiN_1S_3 and NiS_4. Note that NiN_4 and NiN_3S_1 have been successfully synthesized and performed well in electrochemical conditions.[37] Metal-free N_2S_2 porphyrin with *para*-position S atoms has also been successfully synthesized in a previous experiment,[38] while the adjacent S coordinated porphyrin has not been reported yet. Therefore, NiN_2S_2 may also be available experimentally and able to work steadily under electrochemical conditions. Based on the above-mentioned analyses, we mainly focused on NiN_4, NiN_3S_1, and NiN_2S_2 in the following investigation.

To understand the N,S coordination effect, the electronic structures of NiN_4, NiN_3S_1, and NiN_2S_2 were investigated using

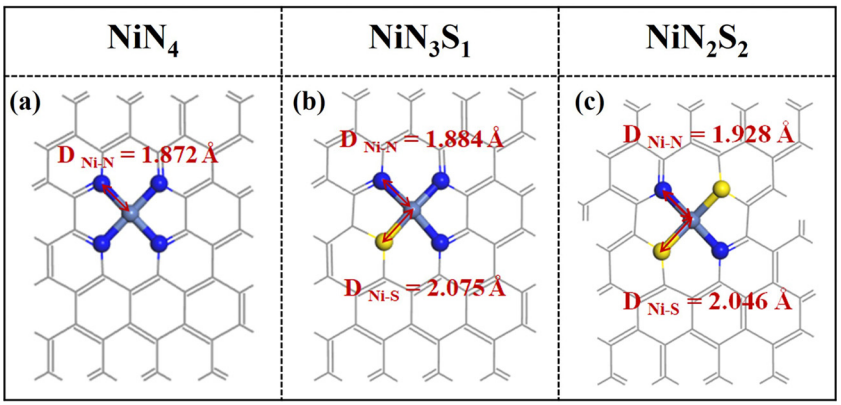

Fig. 1 Optimized structures of (a) NiN_4, (b) NiN_3S_1 and (c) NiN_2S_2.

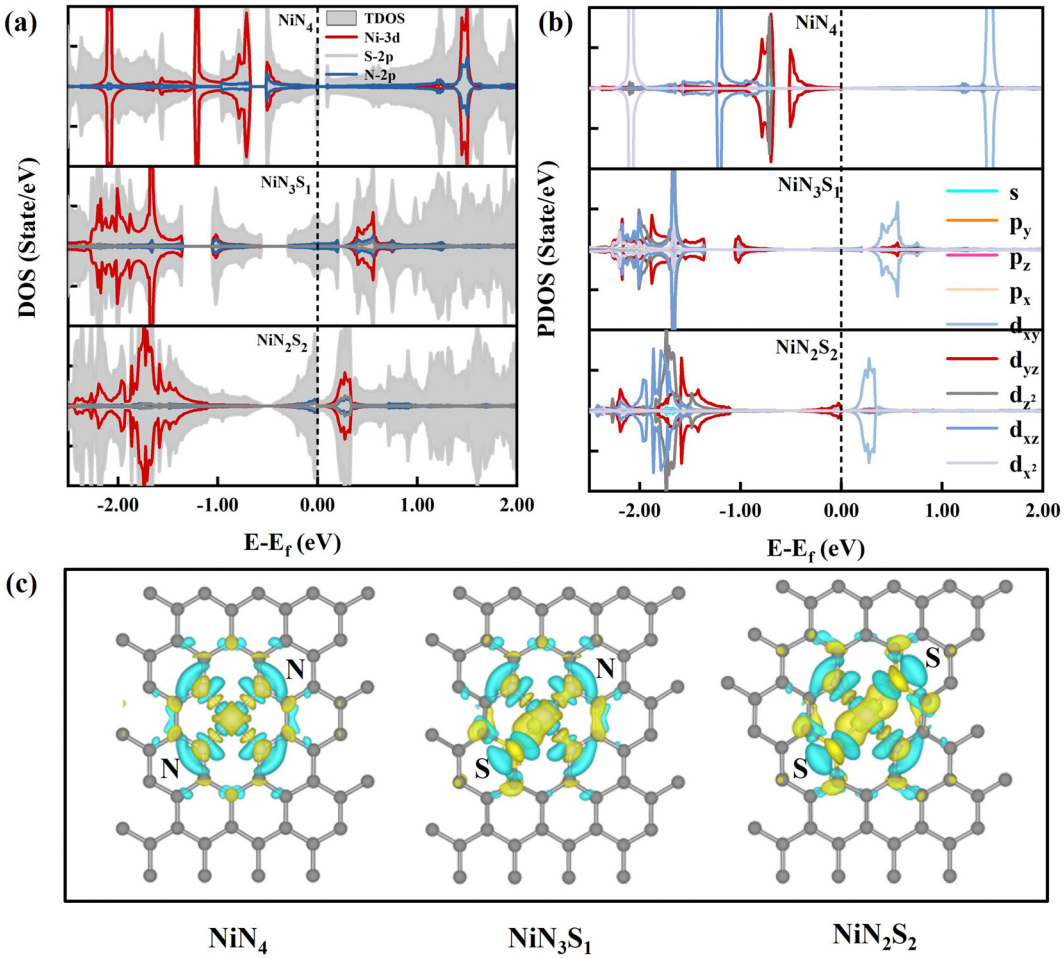

Fig. 2 Electronic structure analysis. (a) Electronic density of states (DOS) and (b) electron projected density of state (PDOS) of NiN_4, NiN_3S_1 and NiN_2S_2. Charge density differences of (c) NiN_4, NiN_3S_1 and NiN_2S_2. Yellow and cyan regions represent increased and decreased electron densities, respectively, and the isosurface values are 2×10^{-3} e Bohr^{-3}.

electronic density of states (DOS) and charge density differences. As shown in Fig. 2a, a large amount of new peaks appear at around −1.60 eV in NiN_3S_1 and NiN_2S_2 but are not observed in NiN_4, which indicates that the substitution of S atoms has great potential to promote intramolecular electron transfer in these SAC catalysts. As shown in Fig. 2b, the peaks of NiN_3S_1 at around −1.60 eV are mainly contributed by the d_{xz}, d_{z^2}, and d_{yz} orbitals of Ni. For NiN_2S_2, the characteristic peaks are mainly contributed by the Ni d_{xz}, d_{z^2}, and d_{yz} orbitals, which are more likely to hybridize with the electron orbitals of intermediates and are thus beneficial to the adsorption of intermediates in the z direction of the Ni atom.[39] The charge density differences in Fig. 2c show that electrons in NiN_4 would transfer from the Ni atom and N atoms to the Ni–N bonds, forming stable Ni–N bonds. In NiN_3S_1 and NiN_2S_2, a large amount of electrons are activated in the Ni atom, which are beneficial to the activation and further conversion of the reactant at the Ni site. More electrons are observed to accumulate at the Ni–S bonds relative to the Ni–N bonds, indicating the stronger interactions between Ni and S atoms than between Ni and N atoms. The charge density differences of the other structures doped with S atoms are shown in Fig. S2 (ESI†). Similar phenomena are observed in NiN_2S_2-1, NiN_1S_3, and NiS_4. To sum up, analyses of the charge density differences and DOS demonstrate that the N,S coordination can provide substrates with a favorable electronic structure for SACs.[40]

3.2 CO_2RR to give CO and HCOOH *via* a two-electron pathway

The adsorption and initial activation of intrinsically inert CO_2 is the primary step of the CO_2RR.[41] A stable CO_2 adsorption configuration would significantly improve the activation of CO_2 and its subsequent reduction. The optimized adsorption configurations and adsorption energies of CO_2 on NiN_4 under different potentials are presented in Fig. S3 (ESI†). At 0 V, −0.23 V, and −0.54 V, CO_2 is physically adsorbed on the surface of NiN_4; the distance between the CO_2 molecule and the surface is around 3.30 Å. The adsorption energy under 0 V is −0.58 eV, while that at −0.23 V is 0.13 eV lower and that at −0.54 V is −0.06 eV lower than that at 0 V. At −0.84 V, CO_2 is chemically adsorbed on the NiN_4, and the adsorption energy is −0.37 eV due to the slight bulge of the Ni atom. The distance between CO_2 and the surface is 1.99 Å, and O–C–O is 135.95°.

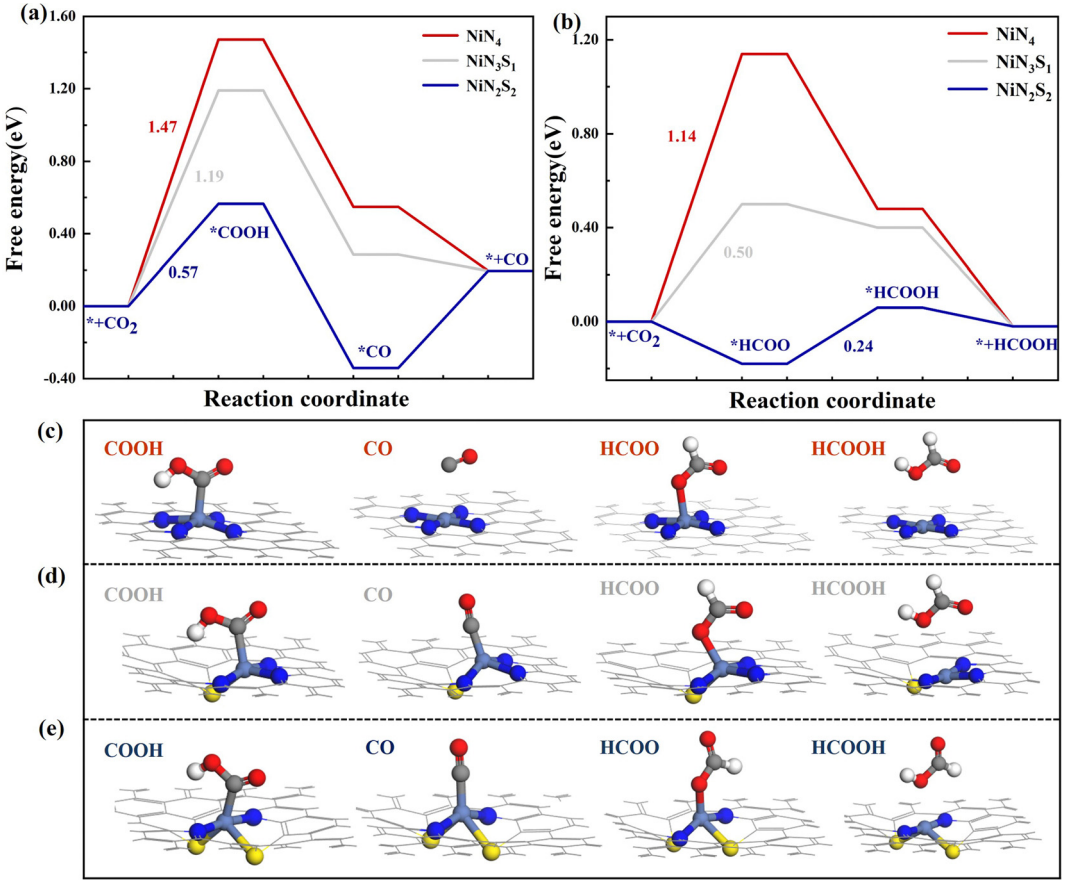

Fig. 3 Free energy profiles of CO_2RR to give (a) CO and (b) HCOOH and the adsorption configurations of the corresponding intermediates on (c) NiN_4, (d) NiN_3S_1, and (e) NiN_2S_2.

In the CO_2RR process, the most accessible products are CO and HCOOH *via* two-electron pathways. Under neutral conditions, the most competitive pathways to form CO and HCOOH on NiN_4, NiN_3S_1 and NiN_2S_2 are presented in Fig. 3, together with their corresponding configurations. A plethora of experimental studies have confirmed that NiN_4 and the corresponding S doping structures mainly produce CO and HCOOH, so we did not further calculate the subsequent reactions of the CO_2RR.[17,19,42–44]

As shown in Fig. 3a, the CO_2RR to give CO tends to proceed along the path CO_2 → *COOH → *CO → CO. Fig. 3c–d present the most stable configurations along the CO_2RR pathways on NiN_4, NiN_3S_1, and NiN_2S_2. On NiN_4, a large free energy change ΔG of 1.47 eV is required for the initial protonation of CO_2 to form the intermediate *COOH. This large ΔG value indicates that it is difficult to form *COOH. The subsequent process *COOH → *CO is favorable with a ΔG of -0.95 eV, followed by a ΔG of −0.64 eV for the desorption of CO. On NiN_3S_1, similar processes to those on NiN_4 are observed, with a smaller ΔG of 0.28 eV for the formation of the *COOH intermediate. For NiN_2S_2, the CO_2 → *COOH reaction requires a ΔG of 0.57 eV, which is 0.90 eV smaller than that on NiN_4. The reaction of *COOH to *CO proceeds along a downhill energy step, and the ΔG value is −0.91 eV. The desorption of CO requires a ΔG of 0.53 eV. Evidently, the potential determining step (PDS) for CO production is the initial protonation of CO_2 to form *COOH on NiN_4, NiN_3S_1 and NiN_2S_2. For the CO_2RR to give CO, NiN_2S_2 exhibits an advantage over NiN_4 and NiN_3S_1.

In the HCOOH production process, the reactions proceed *via* the CO_2 → *HCOO → *HCOOH → HCOOH pathway. As shown in Fig. 3b, on the pristine NiN_4, the reaction CO_2 → *HCOO requires a ΔG of 1.14 eV, which represents the PDS in the HCOOH production process. The reaction of *HCOO to HCOOH proceeds *via* two continuous downhill energy steps with ΔG values of −0.66 and −0.43 eV. For NiN_3S_1, the CO_2 to *HCOO step requires a ΔG of 0.50 eV, which is 0.64 eV smaller than that for NiN_4. The protonation of CO_2 to *HCOO represents the PDS. The *HCOO → *HCOOH step presents a smooth reaction trend with a ΔG of −0.10 eV, followed by a ΔG of −0.42 eV for the desorption of HCOOH. For NiN_2S_2, the CO_2 to *HCOO step has a ΔG value of −0.18 eV. The *HCOO → *HCOOH step continues the uphill energy trend, with a ΔG value of 0.24 eV. The HCOOH desorption requires a ΔG of −0.08 eV. The reaction of *HCOO to *HCOOH is the PDS, with a ΔG value of 0.24 eV. To sum up, the CO_2RR proceeding *via* the two-electron pathway tends to yield HCOOH rather than CO on NiN_3S_1 and NiN_2S_2, and HCOOH is much more easily achieved on NiN_2S_2 with a relatively lower ΔG of 0.24 eV in the PDS.

Considering that the number and position of the S atoms may influence the CO_2RR performance, we also evaluated the potential of NiN_2S_2-1, NiN_1S_3, and NiS_4 for the CO_2RR, as shown in Fig. S4 (ESI†). The results show that free energy changes ΔG of 1.53, −0.18, and 0.97 eV are required for the initial protonation of $*CO_2$ to form the *COOH intermediate on NiN_2S_2-1, NiN_1S_3, and NiS_4. The reaction of $CO_2 \rightarrow *HCOO$ requires a ΔG value of 1.11, −0.92, and 0.29 eV in the HCOOH production process on NiN_2S_2-1, NiN_1S_3, and NiS_4. For NiN_2S_2-1 and NiS_4, the protonation of CO_2 is the PDS for the formation of CO and HCOOH. However, the desorption of CO or HCOOH is the corresponding PDS on NiN_1S_3. It is evident that the coordination environment of three S atoms and one N atom is conductive to the initial protonation of CO_2. In addition to NiS_4, the ability to activate the CO_2 molecule improves with increasing the number of doped S atoms. Compared with the other S doped structures, due to its overall lower ΔG and lowest PDS, NiN_2S_2 is the most favorable for the formation of CO and HCOOH, and HCOOH is formed prior to CO.

3.3 CO_2RR activity and selectivity evaluation

CO_2 adsorption is the initial and crucial step for the CO_2RR. A stable CO_2 adsorption configuration would significantly improve the activation and further reduction of CO_2.[45] On both the NiN_4 and NiN_3S_1 surfaces, CO_2 prefers to bind at the top site of the Ni atom with adsorption energies of −0.58 and −0.59 eV, as shown in Fig. 4a and Fig. S5 (ESI†). The adsorption energy of CO_2 is −0.68 eV, which is 0.10 and 0.09 eV lower than that on NiN_4 and NiN_3S_1, indicating a more effective improvement of the CO_2 capture ability on NiN_2S_2. U_L can be used as an indicator to evaluate the electrocatalytic performance of the catalysts.[46] Fig. 4b summarizes the U_L values for the CO_2RR toward CO and HCOOH on NiN_4, NiN_3S_1, and NiN_2S_2. The PDS and corresponding free energies for the U_L calculation are shown in Table S3 (ESI†). On NiN_4, the U_L values are −1.14 and −1.47 V in the HCOOH and CO production processes, suggesting that the products appear in the sequence HCOOH > CO. On both NiN_3S_1 and NiN_2S_2, the products appear in the same sequence as on NiN_4, and it is worth noting that the U_L value of NiN_2S_2 is more positive than that of other structures. Fig. S6 (ESI†) summarizes the U_L values, PDS, and corresponding free energies for the CO_2RR toward CO and HCOOH on other structures. Comparatively, NiN_2S_2 exhibits more excellent performances of the CO_2RR to give CO and HCOOH than NiN_3S_1 and NiN_4, especially for HCOOH.

The possibility of the HER, as a side reaction of the CO_2RR, must be taken into consideration due to its intense competition with the CO_2RR, which is caused by their similar thermodynamic equilibrium potentials. As shown in Fig. S5 (ESI†), the H atom prefers to be adsorbed at the top site of N

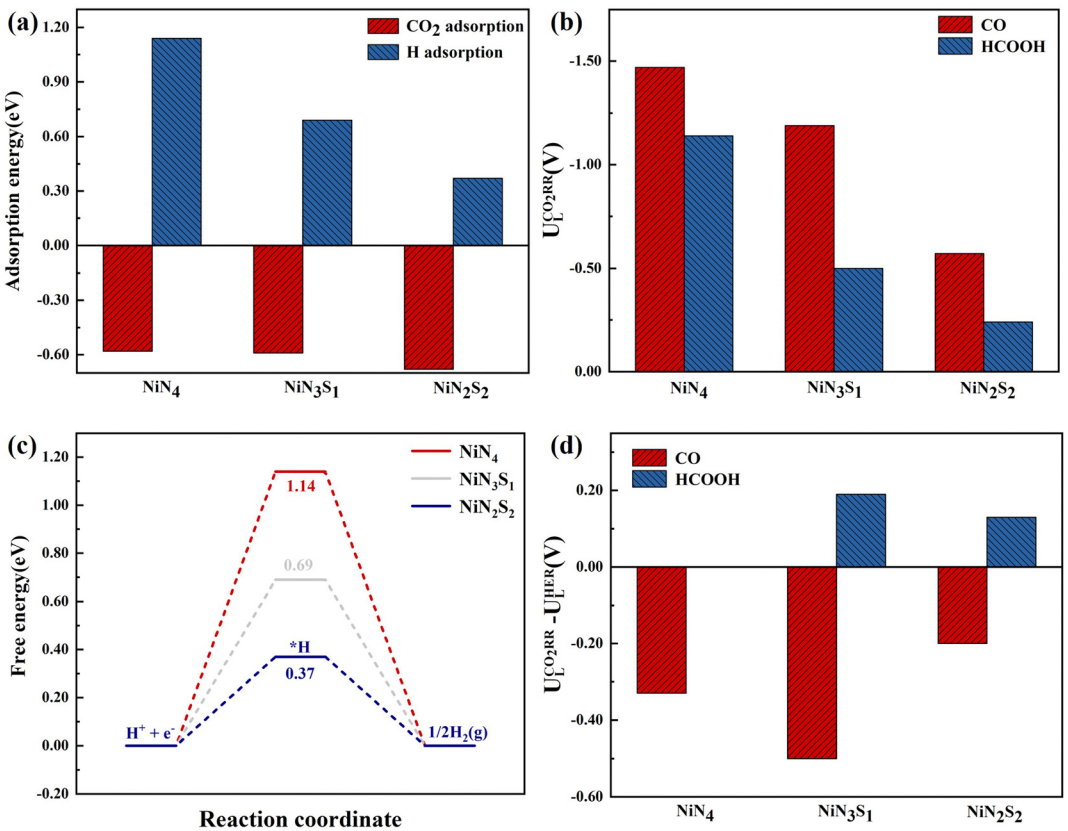

Fig. 4 (a) CO_2 and H adsorption energies on NiN_4, NiN_3S_1 and NiN_2S_2. (b) Free energy diagram of the hydrogen evolution reaction on NiN_4, NiN_3S_1 and NiN_2S_2 (at 0 V *vs.* reversible hydrogen electrode). (c) Summary of the limiting potential $\left(U_L^{CO_2RR}\right)$ of the products for CO and HCOOH production on NiN_4, NiN_3S_1 and NiN_2S_2. (d) Limiting potential difference between CO_2RR and HER $\left(U_L^{CO_2RR} - U_L^{HER}\right)$.

rather than Ni on NiN_4[47] with an adsorption energy of 1.14 eV, which is 1.72 eV less stable than that of CO_2. Therefore, the adsorption of H is far less competitive than that of CO_2 on NiN_4. On NiN_3S_1, the H atom can be adsorbed more stably at N than the Ni site, with an adsorption energy of 0.69 eV. The adsorption of the H atom at the N site is 1.28 eV less stable than that of CO_2, indicating that the adsorption of CO_2 is more competitive than that of H. For NiN_2S_2, the adsorption energy of the H atom at the N site is 0.37 eV, which is 1.05 eV less stable than that of CO_2, indicating that CO_2 adsorption is more competitive. Generally, an ideal electrocatalyst for the CO_2RR should not only possess a high CO_2 conversion performance, but also have excellent HER inhibition ability.[48] Achieving these properties requires that the electrocatalysts have suitable active sites for the initial adsorption of CO_2 rather than H. Here, NiN_4, NiN_3S_1, and NiN_2S_2 electrocatalysts evidently display these merits, which guarantees that CO_2 can occupy the active sites rather than H. Therefore, the CO_2RR is likely to be the primary reaction. We further compare the free energy profiles of the formation of *H on NiN_4, NiN_3S_1, and NiN_2S_2, as shown in Fig. 4c. The H atom tends to be adsorbed at the top site of N, which is determined to be the active site for *H formation. The reaction of $H^+ + e^- \rightarrow$ *H has ΔG values of 1.14, 0.69, and 0.37 eV on NiN_4, NiN_3S_1, and NiN_2S_2, respectively, suggesting that the reaction is easiest to perform on NiN_2S_2. Therefore, it is likely to generate adsorbed H atoms on N near Ni on NiN_2S_2, which can be transferred to CO_2 to promote the hydrogenation reaction. To sum up, the substitution of two S atoms in NiN_4 can further facilitate the protonation of adsorbed intermediates and accelerate the overall CO_2RR compared to other S doped structures.

We further compared the limiting potential difference between the CO_2RR and HER $\left(U_L^{CO_2RR} - U_L^{HER}\right)$ in Fig. 4d, which can effectively elucidate the selectively between the CO_2RR and HER. A more positive value indicates higher CO_2RR selectivity relative to the HER. NiN_2S_2 exhibits more positive $U_L^{CO_2RR} - U_L^{HER}$ values and thus more considerable CO_2RR competition toward both CO and HCOOH than NiN_3S_1 and NiN_4. Therefore, NiN_2S_2 might be a superior CO_2RR electrocatalyst. Fig. S6 (ESI†) compares the limiting potential difference between the CO_2RR and HER on NiN_2S_2-1, NiN_1S_3, and NiS_4. The limiting potential difference between the CO_2RR and HER are shown in Table S4 (ESI†). The result reveals that the products appear in the sequence HCOOH > CO on NiN_2S_2-1, NiN_1S_3, and NiS_4. To sum up, N,S coordination can effectively decrease the U_L of the CO_2RR and improve the electrocatalytic performance, rendering it a promising support material for SACs. NiN_2S_2 was determined to be a promising CO_2RR catalyst for the production of HCOOH with considerable activity and selectivity.

Compared with previous calculations and experimental works with U = 0, it can be found that the NiN_4 and NiN_3S_1 calculated in this work have similar adsorption configurations, free energy change diagrams, and U_L values of the CO_2RR to those reported in the references. The accuracy of the calculated results is further explained.[19,22,37,42,49]

We compared the U_L for the CO_2RR to give HCOOH on NiN_2S_2 with that on SACs[50,51] and Cu-based electrocatalysts.[52] FeN_4–C was predicted to possess a U_L of −0.69 V by DFT calculations.[51] Cu_2O was found to possess a FE_{HCOOH} of 97.7% at −0.64 V in an experiment.[52] Other electrocatalysts in previous studies presented U_L values ranging from −1.14 to −0.74 V.[18,53,54] Here, on NiN_2S_2, the U_L for HCOOH generation is −0.24 V, which is lower than that on most CO_2RR electrocatalysts. Thus, NiN_2S_2 would be an ideal electrocatalyst for HCOOH production. To sum up, N,S coordination can effectively decrease the U_L of the CO_2RR to give HCOOH and improve the electrocatalytic performance, rendering it a promising support material for SACs.

4. Conclusions

In summary, we have performed an in-depth theoretical investigation on the N,S coordination effect in CO_2RR by doping different numbers of S atoms in NiN_4.

(1) N,S coordination provides a more stable anchoring site to form Ni SACs than regular N coordination. The substitution of S atoms in NiN_2S_2 and NiN_3S_1 leads to non-coplanar structures and elongated Ni–N distances. NiN_4, NiN_3S_1, and NiN_2S_2 exhibit excellent thermodynamic and electrochemical stability. Electronic structure analyses show that more electrons accumulate in the Ni–S bonds relative to the Ni–N bonds, forming stronger interactions between the Ni and S atoms. Our findings revealed NiN_2S_2 to be a high-performance CO_2RR catalyst to give HCOOH, and revealed that adjusting coordination environment is an effective strategy to design ideal catalysts for the CO_2RR.

(2) NiN_2S_2 possesses better intramolecular electron transfer ability than NiN_3S_1 and NiN_4, which was ascribed to the effect of the number of S atoms substituted into NiN_4 on the performance of the substrate. The additional Ni d_{z^2} orbitals contribution in NiN_2S_2 can effectively tune the binding of CO_2, H and reaction intermediates in the Ni z direction. N,S coordination facilitates the protonation of adsorbed intermediates, and thus accelerates the overall CO_2RR.

(3) CO_2RR proceeding *via* a two-electron pathway tends to yield HCOOH rather than CO. The PDS is the protonation of CO_2 on NiN_4 and NiN_3S_1, while the *HCOO to *HCOOH step is the PDS for NiN_2S_2 with a ΔG value of 0.24 eV, which is smaller than those of the other structures. N,S coordination can effectively decrease the U_L of the CO_2RR. On NiN_4, NiN_3S_1, and NiN_2S_2, the products all follow the sequence HCOOH > CO, and the U_L values are −1.14, −0.50, and −0.24 V for HCOOH. This reveals that two-S-atom substitution in NiN_4 mainly produces HCOOH rather than CO, which further indicates that the coordination environment has an influence on the catalytic performance.

Conflicts of interest

There are no conflicts to declare.

Acknowledgements

This work was supported by the National Natural Science Foundation of China (22101300), Shandong Natural Science Foundation (ZR2020ME053, ZR2020QB027, ZR2022ME105, and ZR2023ME004), Qingdao Natural Science Foundation (23-2-1-232-zyyd-jch), State Key Laboratory of Enhanced Oil Recovery of Open Fund Funded Project (2022-KFKT-28), Major Special Projects of CNPC (2021ZZ01-05), and the Fundamental Research Funds for the Central Universities (22CX03010A, 20CX06007A and 22CX01002A-1).

References

1 Q. Miao, C. Lu, Q. Xu, S. Yang, M. Liu, S. Liu, C. Yu, X. Zhuang, Z. Jiang and G. Zeng, CoN_2O_2 sites in carbon nanosheets by template-pyrolysis of COFs for CO_2RR, *Chem. Eng. J.*, 2022, **450**, 138427.

2 S. Nitopi, E. Bertheussen, S. B. Scott, X. Liu, A. K. Engstfeld, S. Horch, B. Seger, I. E. L. Stephens, K. Chan, C. Hahn, J. K. Nørskov, T. F. Jaramillo and I. Chorkendorff, Progress and Perspectives of Electrochemical CO2 Reduction on Copper in Aqueous Electrolyte, *Chem. Rev.*, 2019, **119**, 7610–7672.

3 Z. Xin, J. Liu, X. Wang, K. Shen, Z. Yuan, Y. Chen and Y. Lan, Implanting Polypyrrole in Metal-Porphyrin MOFs: Enhanced Electrocatalytic Performance for CO_2RR, *ACS Applied Mater. Interfaces*, 2021, **13**, 54959–54966.

4 G. Hai, X. Xue, S. Feng, Y. Ma and X. Huang, High-Throughput Computational Screening of Metal–Organic Frameworks as High-Performance Electrocatalysts for CO2RR, *ACS Cataly.*, 2022, **12**, 15271–15281.

5 S. Banerjee, C. S. Gerke and V. S. Thoi, Guiding CO2RR Selectivity by Compositional Tuning in the Electrochemical Double Layer, *Acc. Chem. Res.*, 2022, **55**, 504–515.

6 S. Cao, Y. Hu, C. Yang, J. Li, H. Chen, S. Wei, S. Liu, Z. Wang, D. Sun and X. Lu, Constructing surface vacancy to activate the stuck MXenes for high-performance CO_2 reduction reaction, *J. CO2 Util.*, 2022, **62**, 102074.

7 M. B. Gawande, K. Ariga and Y. Yamauchi, Single-Atom Prototype Catalysts, *Small*, 2021, **17**, 2101584.

8 C. Zhu, S. Fu, Q. Shi, D. Du and Y. Lin, Single-Atom Electrocatalysts, *Angew. Chem., Int. Ed.*, 2017, **56**, 13944–13960.

9 S. K. Kaiser, Z. Chen, D. Faust Akl, S. Mitchell and J. Pérez-Ramírez, Single-Atom Catalysts across the Periodic Table, *Chem. Rev.*, 2020, **120**, 11703–11809.

10 H. Zhang, Y. Liu, T. Chen, J. Zhang, J. Zhang and X. W. Lou, Unveiling the Activity Origin of Electrocatalytic Oxygen Evolution over Isolated Ni Atoms Supported on a N-Doped Carbon Matrix, *Adv. Mater.*, 2019, **31**, 1904548.

11 S. Vijay, J. A. Gauthier, H. H. Heenen, V. J. Bukas, H. H. Kristoffersen and K. Chan, Dipole-Field Interactions Determine the CO_2 Reduction Activity of 2D Fe–N–C Single-Atom Catalysts, *ACS Catal.*, 2020, **10**, 7826–7835.

12 X. Zhao, Z. H. Levell, S. Yu and Y. Liu, Atomistic Understanding of Two-dimensional Electrocatalysts from First Principles, *Chem. Rev.*, 2022, **122**, 10675–10709.

13 D. Karapinar, T. Ngoc-Huan, D. Giaume, N. Ranjbar, F. Jaouen, V. Mougel and M. Fontecave, FeNC catalysts for CO_2 electroreduction to CO: effect of nanostructured carbon supports, *Sustainable Energy Fuels*, 2019, **3**, 1833–1840.

14 T. Kropp and M. Mavrikakis, Transition Metal Atoms Embedded in Graphene: How Nitrogen Doping Increases CO Oxidation Activity, *ACS Catal.*, 2019, **9**, 6864–6868.

15 A. S. Varela, N. Ranjbar Sahraie, J. Steinberg, W. Ju, H. S. Oh and P. Strasser, Metal-Doped Nitrogenated Carbon as an Efficient Catalyst for Direct CO_2 Electroreduction to CO and Hydrocarbons, *Angew. Chem.*, 2015, **127**, 10908–10912.

16 C. Guo, T. Zhang, X. Liang, X. Deng, W. Guo, Z. Wang, X. Lu and C. M. L. Wu, Single transition metal atoms on nitrogen-doped carbon for CO_2 electrocatalytic reduction: CO production or further CO reduction?, *Appl. Surf. Sci.*, 2020, **533**, 147466.

17 W. Ju, A. Bagger, G. P. Hao, A. S. Varela, I. Sinev, V. Bon, B. Roldan Cuenya, S. Kaskel, J. Rossmeisl and P. Strasser, Understanding activity and selectivity of metal-nitrogen-doped carbon catalysts for electrochemical reduction of CO_2, *Nat. Commun.*, 2017, **8**, 944.

18 C. Guo, T. Zhang, X. Deng, X. Liang, W. Guo, X. Lu and C. M. L. Wu, Electrochemical CO_2 Reduction to C_1 Products on Single Nickel/Cobalt/Iron-Doped Graphitic Carbon Nitride: A DFT Study, *ChemSusChem*, 2019, **12**, 5126–5132.

19 H. B. Yang, S. F. Hung, S. Liu, K. Yuan, S. Miao, L. Zhang, X. Huang, H. Y. Wang, W. Cai, R. Chen, J. Gao, X. Yang, W. Chen, Y. Huang, H. M. Chen, C. M. Li, T. Zhang and B. Liu, Atomically dispersed Ni(I) as the active site for electrochemical CO_2 reduction, *Nat. Energy*, 2018, **3**, 140–147.

20 Y. Zhang, J. Yang, R. Ge, J. Zhang, J. M. Cairney, Y. Li, M. Zhu, S. Li and W. Li, The effect of coordination environment on the activity and selectivity of single-atom catalysts, *Coord. Chem. Rev.*, 2022, **461**, 214493.

21 S. Cao, S. Wei, X. Wei, S. Zhou, H. Chen, Y. Hu, Z. Wang, S. Liu, W. Guo and X. Lu, Can N, S Cocoordination Promote Single Atom Catalyst Performance in CO2RR? Fe-N2S2 Porphyrin versus Fe-N4 Porphyrin, *Small*, 2021, **17**, 2100949.

22 S. Lu, Y. Zhang, M. F. Mady, O. Egwu Eleri, W. Mekonnen Tucho, M. Mazur, A. Li, F. Lou, M. Gu and Z. Yu, Sulfur-Decorated Ni–N–C Catalyst for Electrocatalytic CO2 Reduction with Near 100% CO Selectivity, *ChemSusChem*, 2022, **15**, e202200870.

23 C. Jia, X. Tan, Y. Zhao, W. Ren, Y. Li, Z. Su, S. C. Smith and C. Zhao, Sulfur-Dopant-Promoted Electroreduction of CO_2 over Coordinatively Unsaturated Ni-N_2 Moieties, *Angew. Chem., Int. Ed.*, 2021, **60**, 23342–23348.

24 J. P. Perdew, K. Burkr and M. Ernzerhof, Generalized Gradient Approximation Made Simple, *Phys. Rev. Lett.*, 1996, **77**, 3865–3868.

25 G. Kresse and J. Furthmüller, Efficiency of ab-initio total energy calculations for metals and semiconductors using a plane-wave basis set, *Comput. Mater. Sci.*, 1996, **6**, 15–50.

26 S. Grimme, J. Antony, S. Ehrlich and H. Krieg, A consistent and accurate ab initio parametrization of density functional

dispersion correction (DFT-D) for the 94 elements H-Pu, *J. Chem. Phys.*, 2010, **132**, 154104.
27 K. Mathew, R. Sundararaman, K. Letchworth-Weaver, T. A. Arias and R. G. Hennig, Implicit solvation model for density-functional study of nanocrystal surfaces and reaction pathways, *J. Chem. Phys.*, 2014, **140**, 084106.
28 J. A. Gauthier, C. F. Dickens, H. H. Heenen, S. Vijay, S. Ringe and K. Chan, Unified Approach to Implicit and Explicit Solvent Simulations of Electrochemical Reaction Energetics, *J. Chem. Theory Comput.*, 2019, **15**, 6895–6906.
29 J. A. Gauthier, S. Ringe, C. F. Dickens, A. J. Garza, A. T. Bell, M. Head-Gordon, J. K. Nørskov and K. Chan, Challenges in Modeling Electrochemical Reaction Energetics with Polarizable Continuum Models, *ACS Catal.*, 2018, **9**, 920–931.
30 A. A. Peterson, F. Abild-Pedersen, F. Studt, J. Rossmeisl and J. K. Nørskov, How copper catalyzes the electroreduction of carbon dioxide into hydrocarbon fuels, *Energy Environ. Sci.*, 2010, **3**, 1311–1315.
31 J. K. Nørskov, J. Rossmeisl, A. Logadottir and L. Lindqvist, Origin of the Overpotential for Oxygen Reduction at a Fuel-Cell Cathode, *J. Phys. Chem. B*, 2004, **108**, 17886–17892.
32 S. Ringe, C. G. Morales-Guio, L. D. Chen, M. Fields, T. F. Jaramillo, C. Hahn and K. Chan, Double layer charging driven carbon dioxide adsorption limits the rate of electrochemical carbon dioxide reduction on Gold, *Nat. Commun.*, 2020, **11**, 33.
33 S. Vijay, W. Ju, S. Brückner, S.-C. Tsang, P. Strasser and K. Chan, Unified mechanistic understanding of CO_2 reduction to CO on transition metal and single atom catalysts, Nature, *Catalysis*, 2021, **4**, 1024–1031.
34 S. Xu and E. A. Carter, Theoretical Insights into Heterogeneous (Photo)electrochemical CO_2 Reduction, *Chem. Rev.*, 2019, **119**, 6631–6669.
35 B. W. J. Chen, L. Xu and M. Mavrikakis, Computational Methods in Heterogeneous Catalysis, *Chem. Rev.*, 2021, **121**, 1007–1048.
36 X. Guo, S. Lin, J. Gu, S. Zhang, Z. Chen and S. Huang, Simultaneously Achieving High Activity and Selectivity toward Two-Electron O_2 Electroreduction: The Power of Single-Atom Catalysts, *ACS Catal.*, 2019, **9**(12), 11042–11054.
37 Y. Hou, M. Qiu, M. G. Kim, P. Liu, G. Nam, T. Zhang, X. Zhuang, B. Yang, J. Cho, M. Chen, C. Yuan, L. Lei and X. Feng, Atomically dispersed nickel-nitrogen-sulfur species anchored on porous carbon nanosheets for efficient water oxidation, *Nat. Commun.*, 2019, **10**, 1392.
38 W. Yan, S. Cao, Z. Xiao, F. Dai, T. Xing, Z. Li, Y. Chen, X. Lu and X. Li, Novel heteroatom sulfur porphyrin organic polymer as a metal-free electrocatalyst for acidic oxygen reduction reaction, *Electrochim. Acta*, 2021, **377**, 138107.
39 Y. Lu, F. Lu, Z. Yang, J. Wu, H. Yu, X. Xie, J. Xu, F. Cheng, J. Chen, K. Xiong, H. Liu, W. H. Wang, J. Zhao and W. Wang, Elucidating orbital selective catalytic activity in brownmillerite Ca2Mn2O5, *AIP Adv.*, 2016, **6**, 095210.
40 M. Liu, W. Zou, J. Cong, N. Su, S. Qiu and L. Hou, N, S Co-Coordinated Mo Defect Sites in Metal Coordination Polymers for Boosting Perdurable and High-Efficiency Alkaline Hydrogen Evolution, *ACS Sustainable Chem. Eng.*, 2023, **11**, 5250–5261.
41 Y. Y. Birdja, E. Pérez-Gallent, M. C. Figueiredo, A. J. Göttle, F. Calle-Vallejo and M. T. M. Koper, Advances and challenges in understanding the electrocatalytic conversion of carbon dioxide to fuels, *Nat. Energy*, 2019, **4**, 732–745.
42 X. Zhao, S. Huang, Z. Chen, C. Lu, S. Han, C. Ke, J. Zhu, J. Zhang, D. Tranca and X. Zhuang, Carbon nanosheets supporting Ni–N_3S single-atom sites for efficient electrocatalytic CO_2 reduction, *Carbon*, 2021, **178**, 488–496.
43 B. Lu, Q. Liu and S. Chen, Electrocatalysis of Single-Atom Sites: Impacts of Atomic Coordination, *ACS Catal.*, 2020, **10**, 7584–7618.
44 G. Ma, G. Ning and Q. Wei, S-doped carbon materials: Synthesis, properties and applications, *Carbon*, 2022, **195**, 328–340.
45 F. Xu, K. Meng, B. Zhu, H. Liu, J. Xu and J. Yu, Graphdiyne: A New Photocatalytic CO2 Reduction Cocatalyst, *Adv. Funct. Mater.*, 2019, **29**, 1904256.
46 S. Cao, S. Zhou, H. Chen, S. Wei, S. Liu, X. Lin, X. Chen, Z. Wang, W. Guo and X. Lu, How can the Dual-atom Catalyst FeCo–NC Surpass Single-atom Catalysts Fe–NC/Co–NC in CO_2RR? – CO Intermediate Assisted Promotion via a Synergistic Effect, *Energy Environ. Mater.*, 2023, **6**, e12287.
47 A. L. Maulana, A. G. Saputro, Y. Prasetyo, M. H. Mahyuddin, M. Iqbal, H. T. Yudistira, I. G. Wenten and H. K. Dipojono, Two-Electron Electrochemical Reduction of CO_2 on B-Doped Ni–N–C Catalysts: A First-Principles Study, The, *J. Phys. Chem. C*, 2021, **125**, 19247–19258.
48 J. Hussain, H. Jónsson and E. Skúlason, Calculations of Product Selectivity in Electrochemical CO_2 Reduction, *ACS Catal.*, 2018, **8**, 5240–5249.
49 Z. Fu, Q. Li, X. Bai, Y. Huang, L. Shi and J. Wang, Promoting the conversion of CO_2 to CH_4 via synergistic dual active sites, *Nanoscale*, 2021, **13**, 12233–12241.
50 X. Zu, X. Li, W. Liu, Y. Sun, J. Xu, T. Yao, W. Yan, S. Gao, C. Wang, S. Wei and Y. Xie, Efficient and Robust Carbon Dioxide Electroreduction Enabled by Atomically Dispersed $Sn^{\delta+}$ Sites, *Adv. Mater.*, 2019, **31**, 1808135.
51 S. Liu, L. Cheng, W. Wang, K. Li, Y. Wang and Z. Wu, Fe-porphyrin carbon matrix as a bifunctional catalyst for oxygen reduction and CO_2 reduction from theoretical perspective, *Mol. Phys.*, 2018, **117**, 1805–1812.
52 J. Li, Y. Kuang, Y. Meng, X. Tian, W.-H. Hung, X. Zhang, A. Li, M. Xu, W. Zhou, C.-S. Ku, C.-Y. Chiang, G. Zhu, J. Guo, X. Sun and H. Dai, Electroreduction of CO_2 to Formate on a Copper-Based Electrocatalyst at High Pressures with High Energy Conversion Efficiency, *J. Am. Chem. Soc.*, 2020, **142**, 7276–7282.
53 G. Wen, D. U. Lee, B. Ren, F. M. Hassan, G. Jiang, Z. P. Cano, J. Gostick, E. Croiset, Z. Bai, L. Yang and Z. Chen, Orbital Interactions in Bi-Sn Bimetallic Electrocatalysts for Highly Selective Electrochemical CO_2 Reduction toward Formate Production, *Adv. Energy Mater.*, 2018, **8**, 1802427.
54 T. Cheng, H. Xiao and W. A. Goddard, Reaction Mechanisms for the Electrochemical Reduction of CO_2 to CO and Formate on the Cu(100) Surface at 298 K from Quantum Mechanics Free Energy Calculations with Explicit Water, *J. Am. Chem. Soc.*, 2016, **138**, 13802–13805.